Materials Advances

ROYAL SOCIETY OF CHEMISTRY

PAPER

View Article Online
View Journal | View Issue

Cite this: *Mater. Adv.*, 2024, 5, 7040

Enhanced activity of highly ordered pristine and black anodic TiO_2 nanotubes for high performance supercapacitors†

Farzad Nasirpouri, * Leila Jafari-Foruzin, Amir-Ali Farmani, Elham Hosseinpour and Hassan Yadipour

Received 27th February 2024,
Accepted 29th July 2024

DOI: 10.1039/d4ma00199k

rsc.li/materials-advances

For energy storage systems such as supercapacitors, it is a huge challenge to achieve high energy density. Here we report on the effect of either tube ordering manipulated by two-step anodisation or electrolytic surface reduction of TiO_2 nanotubes (TNTs) on the supercapacitor performance. The microstructure, crystallinity, morphology and chemical composition of TNTs were examined, compared by using X-ray diffraction (XRD), X-ray energy dispersive spectroscopy (EDX) and field emission scanning electron microscopy (FE-SEM). Electrochemical investigations were performed using cyclic voltammetry (CV), galvanostatic charge–discharge (GCD) and electrochemical impedance spectroscopy (EIS). The GCD curves recorded for TNTs grown in different conditions confirmed the quasi-capacitive behaviour of the produced titanium oxide nanotubes. The galvanostatic charge–discharge showed an increase in the value of specific capacitance rising from 22 μF cm^{-2} to 3672 μF cm^{-2} at a current density of 50 μA cm^{-2} in a solution of 1 M KCl. The highest value corresponds to the black TiO_2 owing to a decrease in charge transfer resistance as evidenced by the Nyquist plots. This study reveals the feasibility of one-pot electrochemical production of efficient TiO_2 nanotubes as efficient nanoporous electrodes for supercapacitors.

1. Introduction

Since the beginning of the industrial revolution, most of the world's energy has been supplied by fossil resources such as coal, gas and oil, and the economic growth of countries depends on the consumption of fossil resources.[1] In recent years, there has been a tremendous amount of attention devoted to developing net-zero carbon emissions by 2025 in order to achieve cleaner energy with lower costs, less environmental pollution and sustainability.[2–7] A life cycle of green sustainable renewable energy production requires efficient energy storage devices. One good example for storing such energies is supercapacitors (SCs). SCs are devices at the boundary between dielectric capacitors and batteries whose main difference remains in the charging storage mechanisms. A lot of work has been carried out over recent years to improve the performance of SCs in terms of capacitance value, energy, power density, cycling efficiency and cycling life.[8–12] SCs have attracted much attention due to their properties such as energy storage potential, which leads to higher power density than those of batteries and conventional dielectric capacitors. In a typical SC, a reversible ion adsorption and desorption reaction occurs at the interfaces between electrode materials and electrolytes, which stores and releases energy in successive cycles.[13,14] Metal oxide materials such as titanium oxide have been considered as efficient electrodes for supercapacitor devices because of their outstanding electrochemical properties.[15,16] For capacitor applications, TiO_2 in spite of its low cost, exhibits relatively much lower areal capacitances in a range of 90–120 μF cm^{-2} than those of other transition metal oxides, such as MnO_2 (160 mF cm^{-2}) and RuO_2 (13 mF cm^{-2}), respectively. Therefore, different approaches are needed to enhance the capacitance properties of TiO_2 to achieve practical efficient TiO_2-based supercapacitors.[17] A typical supercapacitor electrode can be made of pure elements, composites or hybrid materials.[18–24] The energy storage mechanism for supercapacitors can be explained using three types of capacitive behaviour, including: (1) electrochemical double-layer capacitors (EDLCs) which use the net electric charge accumulated at the electrode interface, (2) pseudo-capacitors (PC) which develop from quick and reversible surface redox processes, and (3) hybrid capacitors which take advantage of both of the above mechanisms.[25] An important key is to reach supercapacitors with high efficiency. A lot of effort has been made to overcome the aforementioned issue of supercapacitors to be used as future storage device for various low to high scale applications.[26–30]

Faculty of Materials Engineering, Sahand University of Technology, Tabriz, 51335-1996, Iran. E-mail: f_nasirpouri@yahoo.com, nasirpouri@sut.ac.ir

† Electronic supplementary information (ESI) available. See DOI: https://doi.org/10.1039/d4ma00199k

There are two main approaches to enhance the electrochemical capacity and storage stability of SC electrodes. The first approach is to develop nanostructured electrodes with very large effective surface area. SCs represent an intermediate between batteries and capacitors, which can be classified into electrochemical double-layer capacitors and pseudo-capacitors. In electrochemical double-layer capacitors, the chemical reaction does not take place on the electrodes, whereas the charges accumulate at the electrode/electrolyte interface. In contrast, pseudo-capacitors show a high capacity compared to EDLCs, due to the fact that they stimulate reduction reactions occurring near the electrode surface. The energy density of SCs is determined by two factors: electrode capacitance and cell voltage. One of the effective ways to increase their capacity is to develop nanostructured and porous electrodes with increased energy density. The alternative method of making asymmetric/hybrid SCs includes a potential gap introduced between the two types of electrodes to increase the voltage of the whole cell. In the other words, the positive and negative electrodes are made of PC and EDLC materials, respectively. There are two types of asymmetric/hybrid SCs. First, capacitor type electrode/capacitor type electrode SCs (*e.g.*, redox/redox type such as EDLCs/redox type). Second, capacitor type electrode/battery type electrode SCs.[31]

TiO_2 is one of the most diverse oxides studied in functional and device materials applications such as photocatalysis, electrochemical and photoelectrochemical devices, dye-sensitized solar cells and biomedical devices.[32–34] TiO_2 based binary and ternary composites as electrodes have been attempted by many researchers in order to make high performing candidates for supercapacitors.[35–37]

Anodic TiO_2 nanotubes (TNTs) have been the focus of many research studies for years because of the flexible processing of nanotubes with different shapes and dimensions as well as the ease of doping or grafting them with other suitable elements and compounds.[38] In principle, TNTs as one-dimensional TiO_2 nanostructures exhibit high surface area as well as enhance the charge collection and transport. Earlier reports have also revealed that these nanostructures also have suitable light harvesting properties. TNTs are typically fabricated by anodisation of Ti and alloys in a simple manner where the morphology and dimensions of the nanotubes are manipulated solely by tuning the anodisation parameters. The anodising process offers several advantages for the synthesis of TNTs in form in industrial applications as well. Furthermore, two-step anodising results in more ordered and highly uniform TNTs. The enhanced surface area and improved photocatalytic properties of anodised TiO_2 are particularly beneficial for applications in environmental purification, such as air and water treatment, and in energy storage and conversion devices, including batteries and solar cells. Additionally, anodizing is a scalable and cost-effective technique, making it suitable for large-scale and mass production. The produced anodic TNTs exhibit excellent adhesion to the substrate, mechanical stability, and resistance to wear and corrosion, which extends the lifespan and performance of the end products. In particular, the capability of the anodisation process in tuning the TNTs' size and morphology allows for the customization of the TiO_2 properties to meet specific industrial needs, thereby enhancing the versatility and application potential of this method across various sectors.

Due to the large band gap of TiO_2 (3.0–3.2 eV) and the existence of several fast electron–hole recombination centres, the performance of TiO_2-based materials is limited.[39] This finding focused intense research activities on the growth, modification, properties and applications of these one-dimensional nanostructures of titania, *e.g.* nanotubes.[40,41] Several attempts have been made to reduce the bandgap of TiO_2. The anodisation time and temperature can reduce the band gap energy as it changes from 3.2 to 2.92 eV during two-step anodisation.[42] Zhen-Kun He *et al.* have developed TNTs as a current collector for supercapacitors.[43] The results show that the morphology of TiO_2 can affect the amount of nitrogen doping. Due to the improved charge transfer and the unique free static nanorod structure, the optimized nitrided TiO_2 electrode achieves a significant areal capacity, which is much larger than that of the unseeded nitrided TiO_2 electrode. Wu *et al.*[44] used a simple hydrogenation doping method to significantly improve the electronic conductivity and the capacitive performance of TiO_2 nanotube electrodes.

Black (or reduced) TiO_2 nanotubes (TNTs) are an improved titanium oxide based electrocatalyst because of its remarkable electrochemical activity.[45] The improved activity of the black TNTs is attributed to the surface restructuring, and inducing microstructural defects such as oxygen vacancies or Ti^{3+}.[46] Applications of black TiO_2 (reduced TiO_2) were reported in different areas such as photocatalysis, photoelectrochemical sensors, catalysis, lithium-ion rechargeable batteries, and fuel cells.[47,48] Surface modification of reduced TNTs has been accomplished by different methods. The surface area and porosity of the reduced TiO_2 could be manipulated as a result of different synthesis approaches.[49–53] A high photocatalytic efficiency was reported for black or reduced titania treated by ethylene glycol solution at room temperature.[44,47] Chen *et al.* firstly reported that black TiO_2 exhibits a decreased band gap energy down to 1.5 eV.[54] This decrease of the band gap energy improved the electrochemical activity on black TiO_2 electrodes. A. Chatzitakis *et al.*[53] reported a new method of synthesis of black TiO_2 in the form of nanotubes. In another study, amorphous TiO_2 nanotubes (TNTs) were annealed and reduced in the presence of CaH_2, where they were able to achieve control over the preferred crystal orientation by a simple manipulation.[55] Also, TNTs treated by electrochemical hydrogenation doping (H-TNT) have been employed in supercapacitors. H-TNTs exhibit an improved specific (areal) capacitance at a scan rate of 100 mV s^{-1} (11.8 mF cm^{-2}).[56] The modified electrodes display improved areal capacitance compared to pure TNTs. Lu *et al.* reported that hydrogenated black TiO_2 nanotube arrays obtained by heating anodised TiO_2 nanotubes under a hydrogen environment between 300 to 600 °C exhibit an improved performance as supercapacitors due to increased densities of carriers and hydroxyl groups on the TiO_2 surface from the hydrogenation.[57] In brief, the increased performance as electrode materials for supercapacitor applications using black TiO_2 nanomaterials was suggested to be due to increased densities of charge carriers and hydroxyl groups on the TiO_2 surface

Table 1 Performance comparison of some supercapacitors based on TNT

Electrode material	Specific capacitance (or areal capacitance) (C_S)	Electrolyte	Ref.
TNT-R	9.8 μF cm^{-2}@50 mV s^{-1}	KCl 1 M	This work
Nitrided TiO_2 nanoparticle	85.7 mF cm^{-2}@10 mV s^{-1}	Na_2SO_4 0.5 M	58
TiO_2/Nb_2O_5 nanotube	37 mF cm^{-2}@1 mV s^{-1}	H_2SO_4 1 M	59
TiO_{2-x}/Ti	81.75 mF cm^{-2}@2 mV s^{-1}	H_2SO_4 1 M	60
TiO_2-LSGO	9.9 mF cm^{-2}@1 mV s^{-1}	PVA/H_2SO_4	61
$Co(OH)_2/TiO_2$	1188 F g^{-1}@100 mV s^{-1}	KOH 1 M	62
TiO_2/rGO NS (Green method)	599.90 F g^{-1}@1 A g^{-1}	H_2SO_4 1 M	63
GO/TiO_2	100 F g^{-1}@5 mV s^{-1}	Na_2SO_4 1 M	64
rGO/TiO_2 nanorod	114.5 F g^{-1}@5 mV s^{-1}	Na_2SO_4 1 M	65
Py700@SFO@CC	421 F g^{-1}@1 A g^{-1}	KOH 6 M	66
$SrCo_{0.9}Fe_{0.1}O_{3-\delta}$@CC//AC@CC	526.6 F g^{-1}@1 A g^{-1}	KOH 1 M	67
Fe_3Mo_3C/Mo_2C@CNT	196.3 F g^{-1}@10 mV s^{-1}	KOH 1 M	68
CoO@$Co_2V_2O_7$	7.58 F cm^{-2}@2 mA cm^{-2}	KOH 3 M	69
Cu_2MoS_4@CC	33.9 mA h g^{-1}@1 A g^{-1}	KOH 3 M	70
rGO–TiO_2 NBs	225@0.125 A g^{-1}	1 M Na_2SO_4	71
Graphene–TiO_2 hybrid	165@5 mV s^{-1}	1 M Na_2SO_4	65
100 ALD TiO_2–G	84@10 mV s^{-1}	1 M KOH	72
3D TiO_2@RGO	397@0.36 A g^{-1}	6 M KOH	73
GA/TiO_2	142.6@5 mV s^{-1}	0.1 M NaCl	74
Anatase TiO_2-reduced graphene oxide	206.7 F@0.5 A g^{-1}	0.5 M Na_2SO_4	75
(TiO_2)–graphene nanocomposite hydrogel	206.7 F@0.5 A g^{-1}	0.5 M Na_2SO_4	76
H-TiO_2/NG	401.7@1 A g^{-1}	1 M KOH	77
Hydrogenated TiO_2 nanotubes	3.24 mF cm^{-2}@100 mV s^{-1}	0.5 M Na_2SO_4	78

and the higher electrical conductivity.[56,57] But it is still a challenge to achieve high capacitance in supercapacitors, which requires the design of electrocatalysts. Table 1 summarises the reported data from several studies from the literature. The highest supercapacitor activity is shown according to the investigations performed in alkali media where the supercapacitor reaction in the alkali media is decayed after long-term cycling. Hence, the study of supercapacitor activity in neutral or near-neutral media is an attractive area for practical applications in the industrial system.

In this work, we investigated two main strategies including (i) morphological evolution based on tube ordering and length and (ii) subsequent electrolytic reduction in ethylene glycol solution at room temperature. The effect of the first-step anodisation time of TNTs on the ordering of the nanotube array and their capacitance of the nanotube of pristine TNTs was investigated. In the next step, the effect of electrolytically reduced TNTs, *i.e.* black TNTs, was investigated. Electrochemical impedance spectroscopy (EIS), galvanostatic charge–discharge and cyclic voltammetry (CV) were used to measure the conductivity of the different nanotubes, and capacitance of the supercapacitor. Either strategy employed here is shown to improve the capacitance of TNTs for high specific capacity supercapacitor applications. The present results show a new approach to prepare highly reactive TNT-based electrocatalysts for SC or similar applications.

2. Materials and methods

2.1. Preparation of the Ti substrate

Ti foils (grade 2, 99.65%) with a thickness of 0.6 mm were purchased and used as the substrate. Ti foils were cut into dimensions of 1 × 2 cm^2 and then ground on sand papers meshed up to 5000 grades. Then, the samples were immersed in HNO_3 and HF (3 : 1 volume ratio) as the chemical etchant and immediately washed with distilled water (DI). Finally, the samples were ultrasonically degreased in acetone, ethanol and deionized (DI) water for 15, 15 and 10 minutes, respectively, and washed in ethanol to remove residual contamination before anodising.

2.2. Preparation of TiO_2 nanotube arrays (TNTs)

TNT electrodes were synthesized by two-step anodic oxidation. The anodisation experiments were carried out in a two-electrode cylindrical cell consisting of Ti foil as the anode and stainless steel (316L SS) as the cathode. The distance between the cathode and the anode was adjusted at 3 cm. An ethylene glycol-based solution containing 0.5% wt NH_4F and 2.5% vol DI water was used as the anodisation electrolyte. The electrolyte was vigorously stirred during anodisation using a magnetic stirrer. All experiments were carried out at room temperature and a constant voltage of 60 V. Current transients were recorded during anodising by a computer-controlled data acquisition system (Mastech, Escort 172). In the first step of anodising, the Ti foils were anodised for 4 or 1 h, respectively, and an oxide layer with the structure of oxide nanotubes was made on the surface of the Ti foils. Then this layer was removed by an ultrasonic method in DI water. Then both samples were anodised for 30 min in the second anodisation step under the same conditions, similar to the first step. After the second step, the sample was cleaned with DI water and dried. The anodised TNTs were dried at 150 °C for 45 min to remove residual organic species and then annealed at 450 °C for 60 min in an oven at a heating rate of 3 °C min^{-1} until the amorphous structure changed to a crystalline structure. The obtained samples were numbered as TNT-4h-30min and TNT-1h-30min respectively. In order to investigate the effect of time on the TNTs in the second step, the Ti foil was anodised for four hours in the first step and one hour in the second step (TNT-4h-1h).

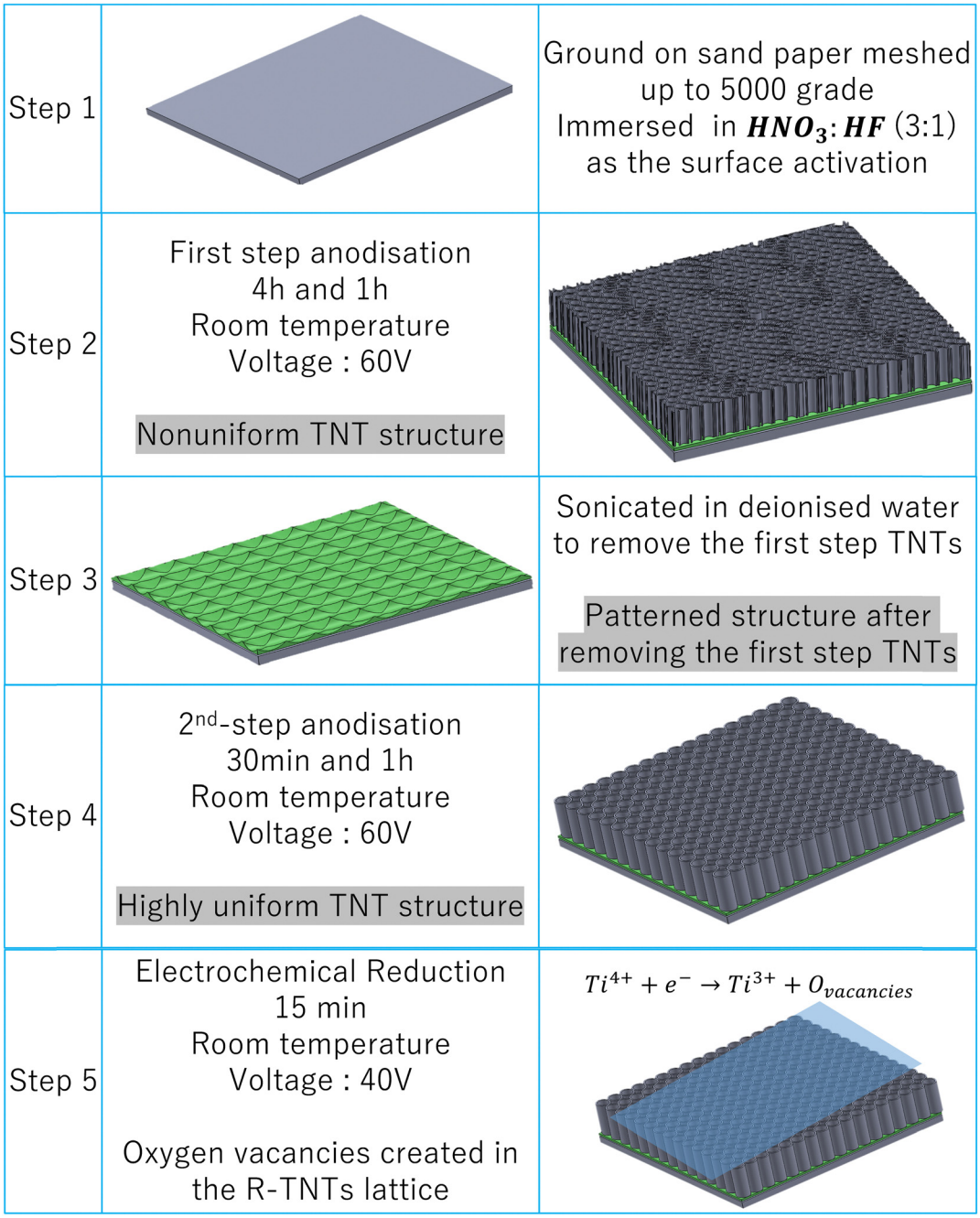

Scheme 1 The preparation of anodic TiO_2 nanotubes (TNTs) and reduced anodic TiO_2 nanotubes (TNT-R).

Scheme 1 systematically shows the process of preparation of the TNTs.

2.3. Preparation of reduced TiO_2 TNTs

As shown in Scheme 1, after the annealing process, TNT-4h-1h was reduced electrochemically at room temperature in a two-electrode system. Anodised TNTs and stainless steel were the cathode and anode, respectively. An ethylene glycol solution consisting of 0.56 wt% NH_4F was used as the reduction electrolyte. The cathodic voltage and the reduction time were fixed at 40 V and 15 minutes, respectively. Finally, the samples were dried for 20 minutes at 80 °C, and named as TNT-R. The conditions for the preparation of the samples are reported in Table 2.

2.4. Morphological and crystalline characterisation

Field-emission scanning electron microscopy (FE-SEM) was used to examine the morphologies of the TNT samples (model MIRA3TESCAN-XMU). The chemical composition was estimated by energy dispersive X-ray spectroscopy (EDS) analysis. The crystalline structure was characterised by X-ray diffraction (XRD) using an X-ray diffractometer (BRUCKERS AXSD &

Table 2 Conditions for preparation of the samples

Sample	First anodisation time (h)	Second anodisation time (min)
TNT-4h-30min	4	30
TNT-1h-30min	1	30
TNT-4h-1h	4	60
TNT-R	4	60

ADVANCE-Germany) with a Cu Kα source in the range of 2θ = 20–80° (λ = 1.54178 A). Field emission scanning electron microscopy (FE-SEM) was used to examine the morphology of the TNT samples. Chemical composition was estimated using energy dispersive X-ray spectrometry (EDS).

2.5. Electrochemical measurements

Electrochemical experiments were carried out by a computer-controlled potentiostat/impedance spectrometer (OrigaFlex-OGF500) using a standard three-electrode system in 1 M KOH electrolyte at room temperature. The active surface was calculated for all three samples and was considered as 1 square centimeter. An $Hg/HgCl_2$ electrode (saturated in KCl), a platinum electrode and a TNT sample were used as the reference, counter and working electrode, respectively. The CV curves of the prepared TiO_2 nanotubes were taken in 1 M KCl solution at a scan rate of 50 mV s^{-1} in the potential range of 0.0 to 5.0 V *vs.* Ag/AgCl. Also, the EIS plots were investigated in 1 M KCl, at the frequency range of 100 kHz to 0.01 Hz. The galvanostatic charge discharge (GCD) analysis was carried out based on chronopotentiometry plots taken on TNT electrodes in a solution of 1 M KCl.

3. Results and discussion

3.1. Morphology and microstructure

3.1.1. Crystallinity of pristine and black TiO_2 nanotubes. Fig. 1(a) and (b) illustrate typical XRD patterns of TNT-4h-1h and TNT-R. The XRD patterns were recorded at angles (2θ) ranging from 10–90°. We find that the crystalline planes of (101), (004), (105), and (116) appeared in Bragg diffraction angles of 25.25, 38, 53.1 and 70.6°, respectively. Most of the peaks are related to a pattern which is compliant with standard card JCPDS no. 1294-44 corresponding to anatase TiO_2. According to the XRD pattern recorded for TNT-4h-1h and TNT-R, it can be seen that there is no change of the crystalline phases for the reduced sample (black) (TNT-R), compared to not pristine TNTs (TNT-4h-1h). However, the intensity of the Bragg diffraction peaks of the TNT-R are higher than those of TNT-4h-1h. This can be attributed to higher crystallinity of TNT-R than TNT-4h-1h. In addition, the peaks of TNT-R have shifted about 0.8° towards a smaller 2θ compared to pristine TNT-4h-1h.

3.1.2. Morphology of pristine and black TiO_2 nanotubes. Fig. 2(a1)–(d2) shows FE-SEM images of the titanium oxide nanotubes. Fig. 2(a1)–(d1) show the top morphology of the titanium dioxide nanotubes. Furthermore, the images taken from cross sections of TNTs produced under different conditions are shown in Fig. 2(a2)–(d2). It is evident that TNTs anodised for

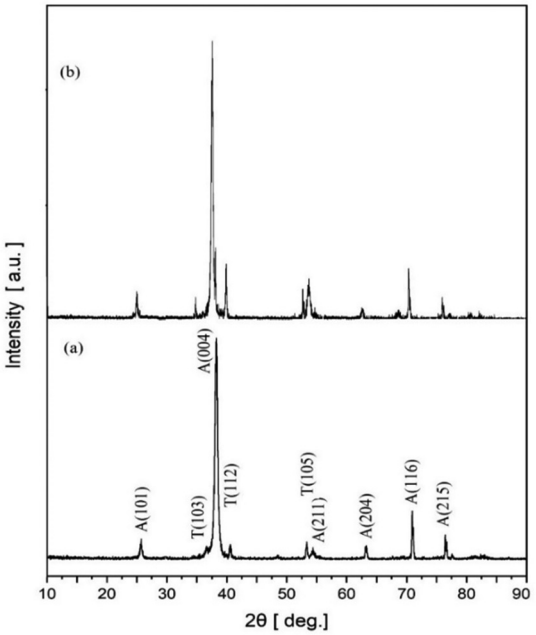

Fig. 1 XRD patterns of (a) titanium nanotubes (TNT-4h-1h) and (b) titanium nanotubes (TNT-R).

1 h in the first step and 30 min in the second step (TNT-1h-30min) exhibit a tube opening diameter of about 79 nm, while the thickness of the tube walls is about 34 nm, see Fig. 2(a1). In contrast, anodisation for a longer time, *i.e.* 4 h, in the first step but for a similar second step time, *i.e.*, 30 min (sample TNT-4h-30min), reveals that the diameter of the nanotube opening is approximately doubled to about 165 nm, whereas the thickness of the nanotube walls is halved to about 20 nm. We have schematically plotted some arbitrary lines on the SEM images to clarify the dimensionality effects of two step anodisation and the time of the first step, as shown in Fig. 2(b1). As is evident in Fig. 2(a1) and (b1), the tube ordering of TNTs increases, which can improve the charge transport as reported previously.[42] Therefore, based on this observation, the effect of increasing the time of the first step of anodic oxidation on the ordering and quality of the growth of nanotubes is clearly visible. With increasing the time of second step anodisation, no change takes place in the tube order of the nanotubes [Fig. 2(c1)].

Fig. 2(a2)–(d2) show the cross-section images of the prepared TiO_2-nanotubes. By comparing the images (a2) and (b2), it can be seen that with the increase in the time of the first step from 1 h to 4 h of the anodic oxidation process, the length of the nanotubes was not changed, so the change time of anodisation at the first step, only caused an increase in the ordering of the nanotubes. But increasing the time of anodisation at the second step [Fig. 2(c2)], from 30 min to 1 h, caused an increase in the length of the nanotubes from 5 to 5.3 μm, and consequently with the increase in the length of the nanotubes, the areal capacity also increases and caused an improvement in TiO_2 activity as a supercapacitor electrode. Furthermore, as shown in Fig. 2(d1), for black or reduced TiO_2-nanotubes, an inner tube diameter of about 134 nm and thickness of the tube

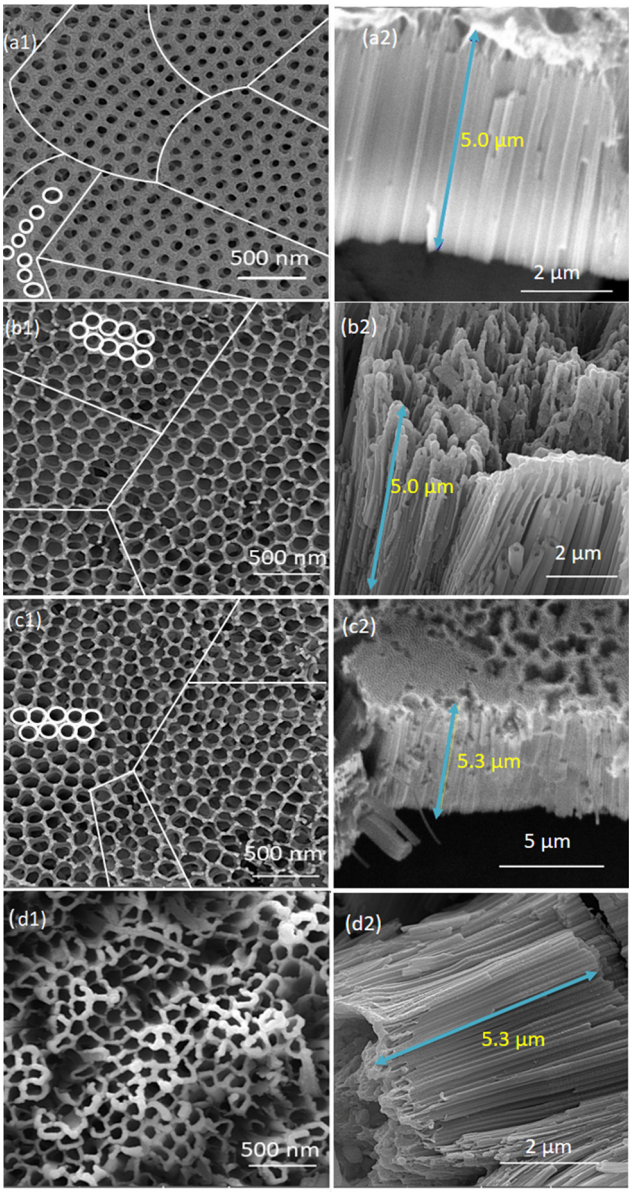

Fig. 2 FE-SEM image of TiO_2 anodised for (a1) TNT-1h-30min, (b1) TNT-4h-30min, (c1) TNT-4h-1h and (d1) reduced TiO_2, and correlated cross section of TiO_2 anodised for (a2) TNT-1h-30min, (b2) TNT-4h-30min, (c2) TNT-4h-1h, and (d2) reduced TiO_2.

walls of about 20 nm are formed. Also, as shown in Fig. 2(d2), the length of the nanotubes for the reduced TiO_2 was not changed compared to the length of pristine TNTs, which were anodised for 1 h (TNT-4h-1h) [Fig. 2(c2)].

3.2. Electrochemical examination of pristine and black TNTs for supercapacitor performance

3.2.1. Cyclic voltammetry (CV) analysis. CV analysis is beneficial to further understanding the electrochemical reactions and their stability for electrochemical processes including supercapacitance. As it can be seen in Fig. 3, TNT-4h-1h has good activity compared to TNT-4h-30min and TNT-1h-30min. This can be attributed to the dimensionality and ordering of the nanotube metal oxide electrodes. In addition, TNT-1h-30min exhibits an improved activity compared to TNT-4h-30min. This can be explained by the fact that we have two nanotubes with different lengths to transfer the charge. When the length of the nanotubes is increased, the effective surface area and the number of charge carriers increase. As a consequence, the electrode–electrolyte interface area increases to carry out oxidation–reduction reactions. On the other hand, with the increase in length, the charge transfer resistance decreases to some extent at first, but from an optimal level onwards, with the increase in the length of the nanotubes, the internal resistance also increases. Thus, two factors interplay in conflict with each other, which prevents further increase of the activity of the supercapacitor, and an increase in the length of the nanotubes causes a decrease in the electrical conductivity.[79,80] Besides, the best electrochemical performance is related to the reduced TiO_2 nanotubes anodised for 4 h in the first step and 1 h in the second step (TNT-R) compared with TNT-4h-30min, TNT-1h-30min, and TNT-4h-1h. This can be attributed to low bandgap energy and microstructural defects such as oxygen vacancies and Ti^{3+} induced by tube ordering.[81,82] According to the electrochemical behaviour examined by CVs (Fig. 3(a) and (b)), the current density of the peaks for the pristine TNTs (TNT-1h-30, TNT-4h-30, and TNT-4h-1h) was lower than those for black or reduced TNTs (TNT-R).

Furthermore, the black or reduced TNTs (TNT-R) exhibit quite different electrochemical performance indicating an electrocatalyst with electrical double layer capacitor (EDLC)-like behaviour. Obviously, black TNTs showed a significantly higher charging current compared to pristine TNTs. This can be attributed to the decrease of the band gap energy owing to the microstructural defects such as oxygen vacancies.[46,83]

Fig. 3(c) presents CV plots of TNT-R recorded at scan rates of 2, 5, 50 and 100 mV s^{-1}. The current density of the CV curves is increased as a function of the scan rate. The shape of the curves is quasi-rectangular, which is characteristic of electrochemical double-layer capacitors (EDLCs). In CV recorded at low scan rates, the presence of redox peaks likely suggests a pseudocapacitive behavior. Considering that titanium dioxide (TiO_2) nanotubes can exhibit both EDLC and pseudocapacitive characteristics depending on the electrolyte and the specific surface treatments, the supercapacitor depicted is likely a hybrid supercapacitor. This type of supercapacitor combines the principles of EDLC and pseudocapacitors to enhance energy storage capacity and power delivery.[84] Based on the CV curves, the highest areal capacitance observed corresponds to TNT-R (reduced TiO_2).

3.2.2. Galvanostatic charge discharge (GCD) analysis. The charging/discharging current density is an important factor for studying the performance of supercapacitors. The results are plotted in Fig. 4(a) and (b) and suggest the reversible behavior of an ideal nanostructured supercapacitor. As shown in Fig. 4(a) and (b), the electrochemical performance of the different TNTs was further studied by galvanostatic charge/discharge measured in the voltage window between 0 and 0.5 V at a current density of 50 µA cm^{-2}. As shown in Fig. 4(a), TNTs completely follow a non-linear behaviour. Fig. 4(b) illustrates the GCD

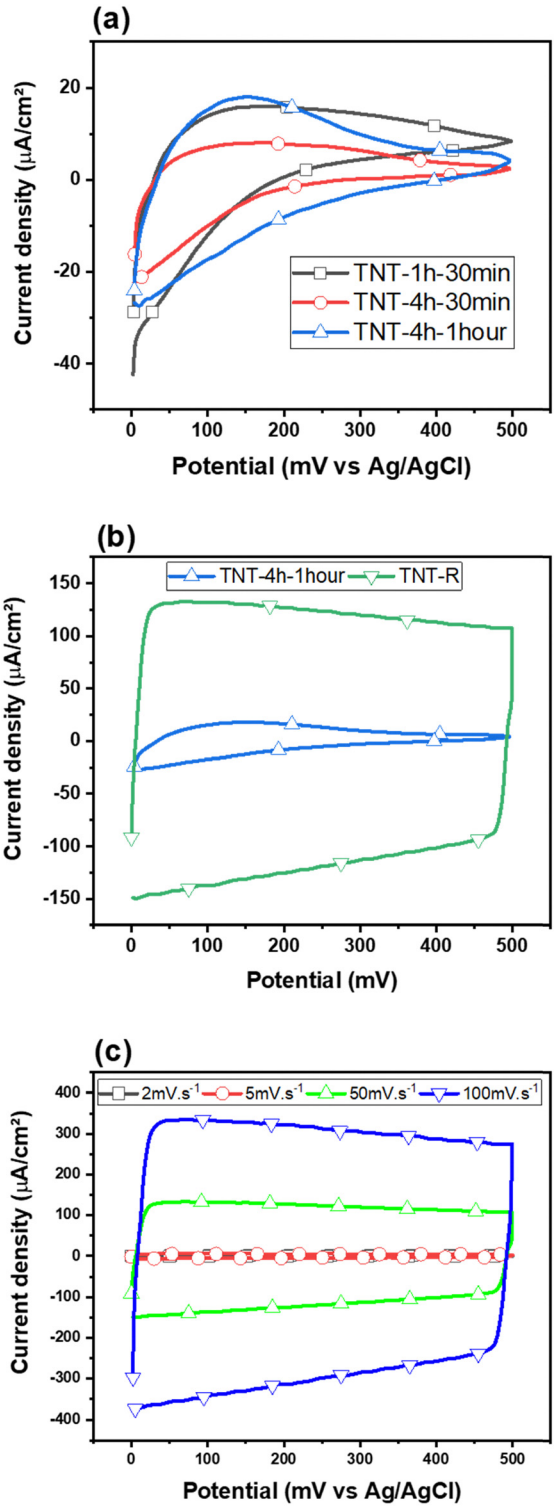

Fig. 3 (a) and (b) Comparison of the cyclic voltammetry diagram related to different conditions of anodic oxidation and electrochemical reduction, and (c) CV curves of TNT-R at scan rate 2, 5, 50 and 100 mV s^{-1}.

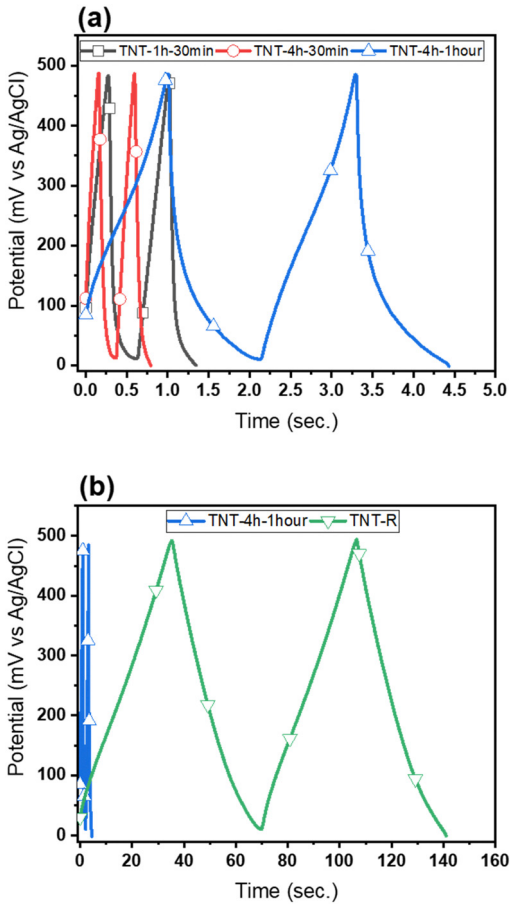

Fig. 4 (a) Charge/discharge profiles of the different TNTs and (b) charge/discharge of the TNT-R and TNT-4h-1h.

curve of TNT-R, which exhibits an isosceles triangle shape. For pseudocapacitive materials, the charging and discharging profiles exhibit non-linear behavior because of quasi-reversible faradaic reactions. The charge/voltage ratio of these faradaic reactions no longer stays constant and changes over time, resulting in a non-symmetric curve.[84] In contrast with other samples, the TNT-R demonstrates superior electrochemical performance as a supercapacitor due to its rapid charge–discharge capability and minimal voltage drop, indicating low internal resistance.

A reason for this could be attributed to the intensification of the redox reactions, which were carried out on the surface of the electrode and electrolyte. This redox reaction is due to the increase of charge carriers. Also, the GCD study is an efficient approach to determine the areal capacitance of electrodes and is frequently used in energy storage devices working at constant current density. Table 3 reports the charge–discharge curves of samples at the current density of 50 μA cm^{-2}. Areal capacitance is estimated using the following formula:[85]

$$C_s = \frac{I\Delta t}{S \cdot \Delta V} \quad (1)$$

where the areal capacitance is C_s (μF cm^{-2}), I (μA) is reported as the constant current during discharge, Δt (s) is shown as the time of discharge, ΔV (V) is known as the potential window, and S (cm^2) is reported as the surface area of the electrode. The areal capacitances of TNT-R, TNT-4h-1h, TNT-1h-30min, and TNT-4h-30min are calculated to be about 3672, 121, 37 and

Table 3 Specific (areal) capacity of different electrodes at a current density of 50 μA cm^{-2} (obtained from GCD)

Electrode	Specific (areal) capacitance (μF cm^{-2}) obtained from GCD
TNT-1h-30min	37
TNT-4h-30min	22
TNT-4h-1h	121
TNT-R	3672

22 μF cm^{-2}, respectively. It can be inferred that the reason for the increased capacitance at TNT-R can be attributed to defects such as oxygen vacancies and low bandgap energy, which improved charge transfer and increased the charge carriers and decreased the recombination rate. Thus, the capacitance and electrical current will be improved. Also, the areal capacitance of TNT-4h-1h is higher than that of TNT-1h-30min, and TNT-4h-30min. This enhanced capacitance can be attributed to enhanced ordering of the tubes as shown by the FE-SEM images, see Fig. 2(c1).

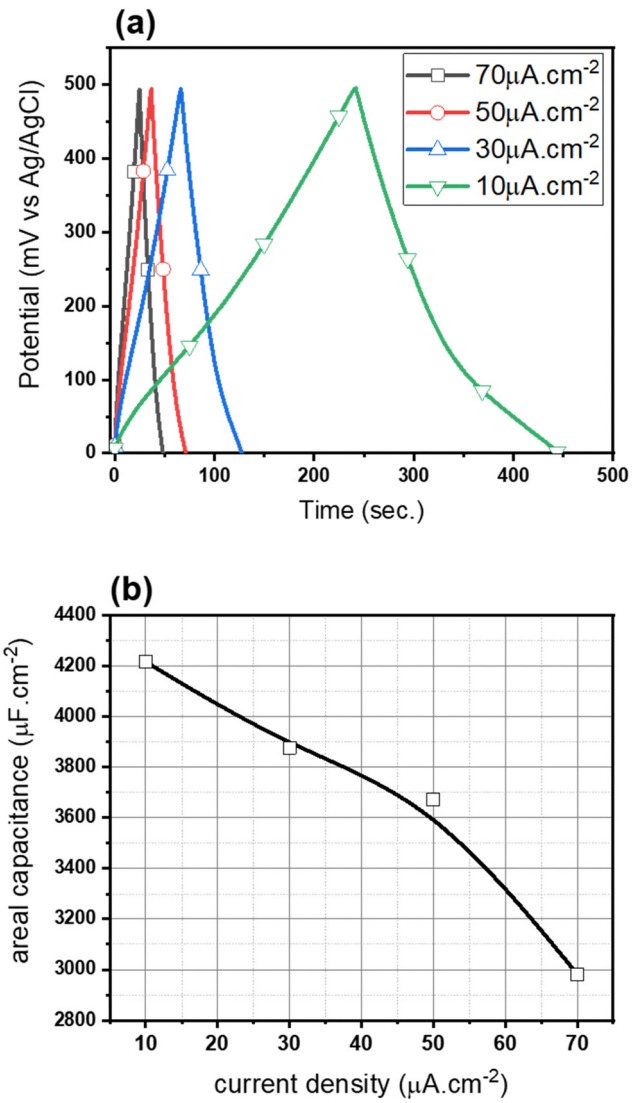

Fig. 5 (a) Galvanostatic charge–discharge curves of TNT-R at different current densities from 10 to 70 μA cm^{-2} and (b) the areal capacitance of TNT-R at different current densities from 10 to 70 μA cm^{-2}.

In Fig. 5(a), electrochemical measurements were reported for the TNT-R at the current density of 10, 30, 50, and 70 μA cm^{-2}. As the current density enhances from 10 to 70 μA cm^{-2}, the areal capacitance of the samples is reduced (Fig. 5(b)).

At a current density of 10 μA cm^{-2}, a significant improvement in areal capacitance is observed for black (reduced) TNTs through electrochemical reduction over other current densities. It is possible that a high current density leads to irreversible processes. Although, a lower current density leads to an improvement in the electrode performance.[86] Moreover, the high stability of the reduced TiO_2 sample was evidenced by the dramatically improved charge storage.

3.2.3. Electrochemical impedance spectroscopy. To further study the electrochemical properties of the different TNT electrodes, we performed electrochemical impedance spectroscopy. Electrochemical impedance spectroscopy (EIS) measurement is a reliable tool to study the charge transfer and recombination rate at semiconductor electrolyte interfaces, where "Z_{re}" is the real part and "Z_{im}" is the imaginary part at the EIS curves. This study is demonstrated based on the Nyquist plot performance in 1 M KOH, at the frequency range of 100 kHz to 0.01 Hz.[87]

Fig. 6 displays the Nyquist plot of the TNTs in a KCl 1 M electrolyte solution, which reveals interesting features of the electrode/electrolyte system. The Nyquist plot in Fig. 6(a) reveals that TNT-R has the lowest electrical resistance compared to the other samples. The equivalent resistance (R_S), seen at the point where the curve meets the horizontal axis reflects the combined resistance of electrolyte ions, electrode materials and electrode–electrolyte interface. The charge transfer resistance (R_{ct}), represented in the circuit by the element labelled "R_{ct}", signifies the resistance specifically at the electrode–electrolyte interface. The high frequency region corresponds to the charge transfer limiting process and is attributed to the double-layer capacitance (C_{dl}) in parallel with the charge transfer resistance (R_{ct}) at the contact interface between the electrode surface and electrolyte solution. This region of the Nyquist plot provides valuable information about the charging and discharging behaviour of the electrodes. However, no semicircle arc was observed for the TNT electrode, as depicted in Fig. 6(a). This suggests that the charge transfer of these working electrodes is excellent and suitable for electrochemical supercapacitor applications, with virtually no indication of electrical resistance. The absence of a semicircle arc in the Nyquist plot is a clear indication of the superior performance of the TNT electrode.

The linear part in the low frequency region is associated with the Warburg resistance (diffusive resistance) of the electrolyte into the interior of the electrode surface and ion diffusion/transport into the electrode surface. This region of the Nyquist plot provides insight into the mass transfer processes that occur during the charging and discharging of the electrodes. Moreover, a line almost vertical to the real axis in the imaginary part of the impedance in the low-frequency region, indicating swift ion diffusion in the electrolyte and adsorption onto the

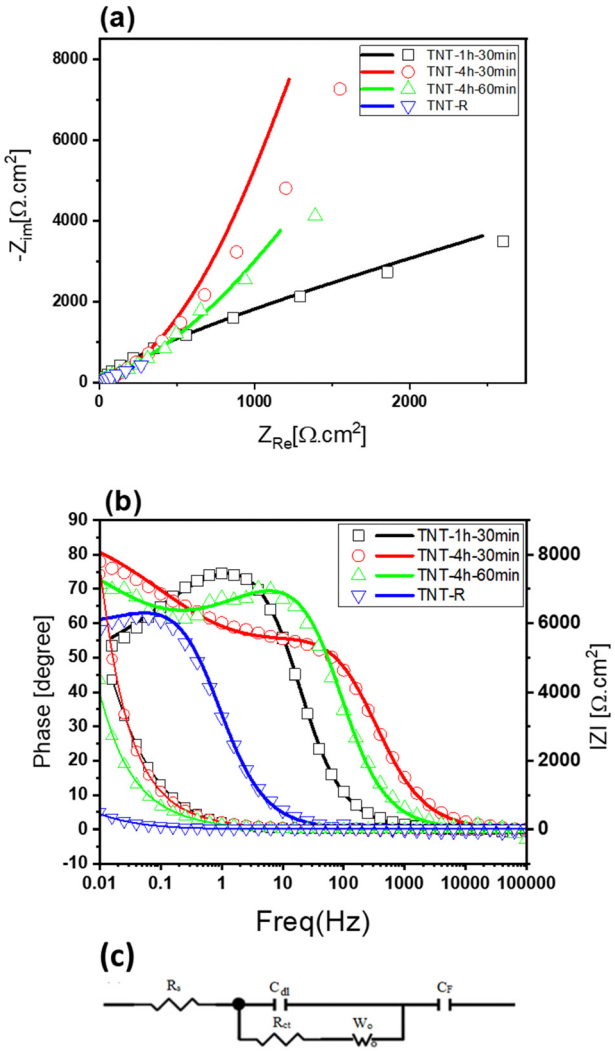

Fig. 6 (a) Nyquist plots of the different TNTs and modeling of equivalent circuits for TNT supercapacitors, (b) Bode and phase plot (line: fitted data) and (c) their equivalent circuit.

electrode surface, suggests an ideal capacitive behaviour of the electrodes. This behaviour is highly desirable for electrochemical supercapacitor applications, as it can result in high power density, fast charging/discharging rates, and long cycle life. The amount of charge transfer resistance in the Nyquist plots gives adequate information about the charge transfer.[44,88,89]

The TNT-4h-1h electrode has a smaller semicircle diameter in comparison with the TNT-1h-30min, and TNT-4h-30min electrodes. Furthermore, TNT-R shows a smaller charge transfer resistance than the other three electrodes. The low R_{ct} at TNT-R can be attributed to low band gap energy, which improved the charge transfer.[90,91] Also, an equivalent electrical circuit is presented in Fig. 6(c). The equivalent circuit was used to analyse the measured electrical impedance of the samples. Also, the results of fitted data are summarised in Table 4. The circuit components and their meanings are:

R_S: equivalent resistance; C_{dl}: double-layer capacitance; W_o: Warburg diffusion element; R_{ct}: charge transfer resistance; C_F: faradaic capacitance.

The R_S values are 13.78, 4.97, 3.432, and 15.07 Ω cm^2, and the R_{ct} values are 0.00062, 0.00013, 0.00057, and 0.0001 Ω cm^2 for TNT samples subjected to different conditions: TNT-1h-30min, TNT-4h-30min, TNT-4h-60min, and TNT-R. As you can see, the sample with the lowest the equivalent resistance (R_S) is TNT-4h-60min, while the sample with the lowest resistance at the electrode–electrolyte interface (R_{ct}) is TNT-R indicating better conductivity and capacitive behaviour. Table 3 demonstrates a significant rise in capacitance with increasing first anodisation time. This can be attributed to the formation of a more extensive network of TNT nanotubes, leading to a reduction in the overall charge transfer resistance (R_{ct}). However, extending the second anodisation time can have an opposing effect. While it may lead to longer TNT nanotubes, their inherent semiconducting nature causes the electron transfer resistance to rise, as shown in Table 4. Additionally, the analysis of the Warburg impedance (W_o) for TNT-R suggests that this configuration offers the easiest access for ions compared to other samples. Interestingly, the analysis of the faradaic capacitance (C_F) for TNT-R reveals that reducing TNT is the most effective approach to enhancing the capacitance of TNT samples. In summary, the Nyquist plots and EIS data provide valuable insights into the performance and behavior of the TNT electrode/electrolyte system. The absence of a semicircle arc in the Nyquist plot indicates excellent charge transfer and ideal capacitive behavior, making the TNT electrode a promising candidate for electrochemical supercapacitor applications.

3.2.4. Stability of TNTs for supercapacitor applications. The study of capacitive stability was investigated on the TNT-R during 1000 cycles of CV at a scan rate of 80 mV s^{-1} (Fig. 7(a)). As shown in Fig. 7(b), TNT-R shows high cycling performance with an areal capacitance drop of less than 29% after 1000 cycles. The degradation of the supercapacitor areal capacitance in TNT-R after 1000 cycles, can be attributed to several factors:[92,93] (i) structural defects and hydrogen diffusion – over time, structural defects and the gradual diffusion of incorporated hydrogen in TNT-R contribute to the loss of capacitance. These structural changes can impair the overall stability and performance of the material during extended cycling, (ii) surface oxygen vacancies (OVs) – treatments that increase the electron donor density by creating surface OVs can negatively impact the stability. Although such treatments can shift the flat-band potential negatively and decrease surface recombination centers and electron-trap state density, they might also introduce instabilities in the material over long-term cycling, (iii) poor electrical conductivity – conventional synthesis

Table 4 The value of various parameters for TNTs obtained from fitting data

Element	R_s (Ω cm^2)	R_{ct} (Ω cm^2)	W_o (mS s^5)	C_{dl} (F)	C_F (F)
TNT-1h-30min	13.78	0.00062	10.26	5.714×10^{-4}	4.67×10^{-8}
TNT-4h-30min	4.97	0.00013	6.864	2.281×10^{-3}	2.542×10^{-3}
TNT-4h-1h	3.432	0.00057	7.10	2.214×10^{-3}	6.377×10^{-3}
TNT-R	15.07	0.00010	10.49	8.24×10^{-3}	0.1998

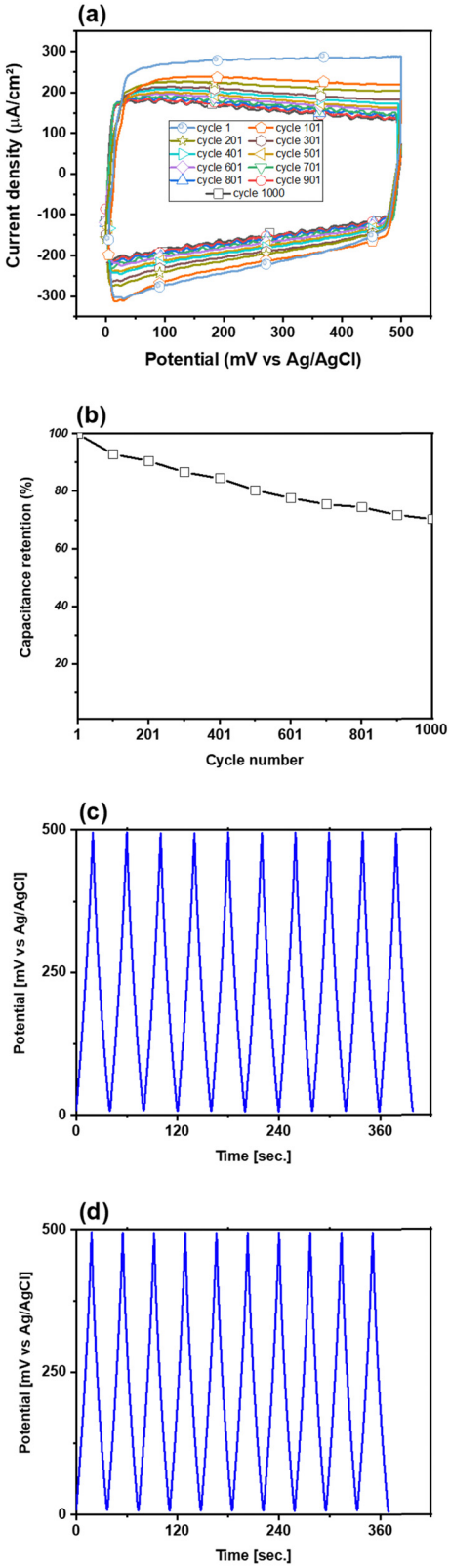

Fig. 7 (a) CV curves at a scan rate of 80 mV s^{-1} (1000 cycle number), (b) areal capacitance retention, (c) charge–discharge curve in the first 10 cycles and (d) charge–discharge curve in the last 10 cycles during 1000 cycles.

methods for TiO_2 result in poor electrical conductivity, which can hinder the performance of supercapacitors. Enhancements in electrical conductivity, such as those achieved by introducing defects (like oxygen vacancies) by reducing TiO_2 by electrochemical methods. These modifications can synergistically improve electrical conductivity, rate capability, and electrochemical stability, leading to better performance. However, if these modifications are not stable over long-term cycling, they can contribute to degradation. The supercapacitor in the provided CV plot is likely a hybrid supercapacitor, utilizing titanium dioxide nanotubes which may exhibit both electrochemical double-layer and pseudocapacitive behaviors. In addition, the charge–discharge curves recorded at a current density of 70 μA cm^{-2} during 1000 cycles are shown in Fig. 7(c) and (d). We observed that over the first ten and the last ten cycles, there are no significant differences, and its stability is significant.

4. Conclusion

Titanium dioxide nanotubes were synthesized by the anodic oxidation method. Then, the effects of ordering, and length of the nanotubes as well as the process of electrochemical reduction on the structure of the nanotubes were studied for their supercapacitor activity. For this purpose, in order to investigate the effect of the ordering of nanotubes, the anodic oxidation process was carried out in two steps for 1 h (TNT-1h-30min) and 4 h (TNT-4h-30min) in the first step. In order to investigate the effect of the length of the nanotubes, the second step of the synthesis process was performed in two times of 30 min (TNT-4h-30min) and 1 h (TNT-4h-1h). According to the results of electrochemical tests, the optimal time of 1 h for the second step was confirmed. An electrochemical reduction process was performed to produce black or reduced TNTs. Three types of electrochemical tests, including cyclic voltammetry, galvanostatic charge–discharge, and electrochemical impedance, were performed on the samples, and the results of all three tests are in complete agreement with each other. We understand that the ordering and length of the nanotubes are effective and efficient in improving the supercapacitor activity and increased the specific capacity, but the effect of the length of nanotubes is greater than that of the other factor. Also, in this method the reduced TiO_2 nanotubes have a specific capacity of 3672 μF cm^{-2} under a current density of 50 μA cm^{-2}.

Data availability

Data reported in this manuscript are mainly extracted from an MSc theses of Elham Hosseinpour and Hassan Yadipour at Sahand University of Technology and Dr Leila Jafari Foruzin's postdoctoral research works. These data will be available on request.

Conflicts of interest

There are no conflicts to declare.

Acknowledgements

The authors are grateful to Sahand University of Technology for financial support.

References

1 P. S. Chen, Y. Hu, S.-Y. Li, M. Mazurkiewicz-Pawlicka and A. Małolepszy, *Int. J. Electrochem. Sci.*, 2024, **19**, 100523.
2 H. Zhou and Y. Zhang, *J. Power Sources*, 2013, **239**, 128–131.
3 M. Ubaidullah, J. Ahmed, T. Ahamad, S. F. Shaikh, S. M. Alshehri and A. M. Al-Enizi, *Mater. Lett.*, 2020, **266**, 127492.
4 G. M. Dias, J. C. Bernardes, B. N. Wesling, D. Müller, L. S. Marques and C. R. Rambo, *Open Ceram.*, 2021, **8**, 100196.
5 A. M. Al-Enizi, J. Ahmed, M. Ubaidullah, S. F. Shaikh, T. Ahamad, M. Naushad and G. Zheng, *J. Cleaner Prod.*, 2020, **248**, 119251.
6 A. M. Al-Enizi, M. Ubaidullah, J. Ahmed, T. Ahamad, T. Ahmad, S. F. Shaikh and M. Naushad, *Composites, Part B*, 2020, **183**, 107655.
7 M. Ubaidullah, A. M. Al-Enizi, T. Ahamad, S. F. Shaikh, M. A. Al-Abdrabalnabi, M. S. Samdani, D. Kumar, M. A. Alam and M. Khan, *J. Energy Storage*, 2021, **33**, 102125.
8 N. Kunthakudee, T. Puangpetch, P. Ramakul, K. Serivalsatit and M. Hunsom, *Int. J. Hydrogen Energy*, 2022, **47**, 23570–23582.
9 G. Song, C. Li, T. Wang, K. H. Lim, F. Hu, S. Cheng, E. Hondo, S. Liu and S. Kawi, *Small*, 2024, **20**, 2305517.
10 A. Tundwal, H. Kumar, B. J. Binoj, R. Sharma, G. Kumar, R. Kumari, A. Dhayal, A. Yadav, D. Singh and P. Kumar, *RSC Adv.*, 2024, **14**, 9406–9439.
11 Y. M. Volfkovich, *J. Electroanal. Chem.*, 2024, 118290.
12 Q. Rong, C. Yuwen, Y. Liu, Y. Liu, C. Wang, Y. Wang, D. Zhang and Z. Wen, *Nano Res.*, 2024, **17**, 4039–4046.
13 P. Liu, Y. Gao, Y. Tan, W. Liu, Y. Huang, J. Yan and K. Liu, *Nano Res.*, 2019, **12**, 2835–2841.
14 Q. Li, N. Mahmood, J. Zhu, Y. Hou and S. Sun, *Nano Today*, 2014, **9**, 668–683.
15 S. Chetana, H. Guddappa, V. N. Thakur, N. Kumar, N. C. Joshi, V. Mirle and M. Shetty, *J. Mater. Sci.: Mater. Electron.*, 2024, **35**, 595.
16 S. Wongprasod, N. Tanapongpisit, P. Laohana, T. M. Huyen Nguyen, H. Q. Van, S. Kim, S. Srikam, S. Sonsupap, N. Chanlek and M. Horprathum, *ACS Appl. Nano Mater.*, 2024, **7**, 6712–6721.
17 W. Pholauyphon, R. N. Bulakhe, J. Praneerad, R. Attajak, J. Manyam, I. In and P. Paoprasert, *Electrochim. Acta*, 2021, **390**, 138805.
18 R. Lakra, R. Kumar, D. Thatoi and A. Soam, *Mater. Today: Proc.*, 2023, **74**, 863–866.
19 R. Lakra, R. Kumar, P. K. Sahoo, D. Thatoi and A. Soam, *Inorg. Chem. Commun.*, 2021, **133**, 108929.
20 N. Liu, X. Zhou, N. T. Nguyen, K. Peters, F. Zoller, I. Hwang, C. Schneider, M. E. Miehlich, D. Freitag and K. Meyer, *ChemSusChem*, 2017, **10**, 62–67.
21 X. Yu, X. Zhang, Y. Lai, D. Wang and Y. Liu, *Green Energy Environ.*, 2022, **7**, 485–491.
22 R. Kumar, B. K. Singh, A. Soam, S. Parida, V. Sahajwalla and P. Bhargava, *Nanoscale Adv.*, 2020, **2**, 2376–2386.
23 A. Soam, K. Parida, R. Kumar and R. O. Dusane, *Ceram. Int.*, 2019, **45**, 18914–18923.
24 S. Hejazi, S. Pour-Ali, M. Killian and S. Mohajernia, *Electrochem. Commun.*, 2022, **136**, 107246.
25 Y. Wang, Y. Song and Y. Xia, *Chem. Soc. Rev.*, 2016, **45**, 5925–5950.
26 R. Lakra, R. Kumar, P. K. Sahoo, D. Sharma, D. Thatoi and A. Soam, *Carbon Trends*, 2022, **7**, 100144.
27 S. Rani, N. Kumar, A. Tandon and Y. Sharma, *IEEE Trans. Electron Devices*, 2020, **68**, 251–256.
28 M. Z. U. Shah, M. S. Javed, M. Sajjad, A. Shah, M. S. Shah, S. ur Rahman, A. Mahmood, M. Ahmad, M. A. Assiri and H. Hou, *J. Sci.: Adv. Mater. Devices*, 2022, **7**, 100418.
29 D. Ghosh, S. Giri, S. Kalra and C. K. Das, *Open J. Appl. Sci.*, 2012, **2**, 70.
30 M. S. Lal, R. Badam, N. Matsumi and S. Ramaprabhu, *J. Energy Storage*, 2021, **40**, 102794.
31 M. Saleem, F. Ahmad, M. Fatima, A. Shahzad, M. S. Javed, S. Atiq, M. A. Khan, M. Danish, O. Munir and S. M. B. Arif, *J. Energy Storage*, 2024, **76**, 109822.
32 H. Cheshideh, E. Moslehifard and F. Nasirpouri, in *Functionalized Nanomaterial-Based Electrochemical Sensors*, ed. C. M. Hussain and J. G. Manjunatha, Woodhead Publishing, 2022, pp. 521–554, DOI: 10.1016/B978-0-12-823788-5.00004-1.
33 F. Nasirpouri, P. s N. S. Peighambardoust, A. Samardak, A. Ognev, V. Korochentsev, I. Osmushko and R. Binions, *ChemElectroChem*, 2017, **4**, 1227–1235.
34 F. Nasirpouri, I. Yousefi, E. Moslehifard and J. Khalil-Allafi, *Surf. Coat. Technol.*, 2017, **315**, 163–171.
35 R. Huang, J. Zhang, Z. Dong, H. Lin and S. Han, *Energy Fuels*, 2022, **36**, 9261–9271.
36 B. Pant, M. Park and S.-J. Park, *Polymers*, 2019, **11**, 899.
37 D. P. Ojha, M. B. Poudel and H. J. Kim, *Mater. Lett.*, 2020, **264**, 127363.
38 A. B. Younis, Y. Haddad, L. Kosaristanova and K. Smerkova, *Wiley Interdiscip. Rev.: Nanomed. Nanobiotechnol.*, 2023, **15**, e1860.
39 A. M. Elshahawy, S. M. Elkatlawy, M. S. Shalaby, C. Guan and J. Wang, *J. Electron. Mater.*, 2023, **52**, 1347–1356.
40 P. Tang, X. Li, C. Xie and X. Xiao, *ACS Appl. Nano Mater.*, 2023, **6**, 410–420.
41 O. Zakir, A. Ait-Karra, R. Idouhli, M. Khadiri, B. Dikici, A. Aityoub, A. Abouelfida and A. Outzourhit, *J. Solid State Electrochem.*, 2023, 1–19.
42 A. Pourandarjani and F. Nasirpouri, *Ceram. Int.*, 2018, **44**, 22671–22679.
43 X. Su, Q. He, Y.-E. Yang, G. Cheng, D. Dang and L. Yu, *Diamond Relat. Mater.*, 2021, **114**, 108168.
44 F. Habibi-Hagh, L. J. Foruzin and F. Nasirpouri, *Int. J. Hydrogen Energy*, 2023, **48**, 11225–11236.
45 H. Sopha, J. Bacova, K. Baishya, M. Sepúlveda, J. Rodriguez-Pereira, J. Capek, L. Hromadko, R. Zazpe, S. M. Thalluri and J. Mistrik, *Surf. Coat. Technol.*, 2023, **462**, 129504.

46 Q. Kang, J. Cao, Y. Zhang, L. Liu, H. Xu and J. Ye, *J. Mater. Chem. A*, 2013, **1**, 5766–5774.
47 Z. Li, H. Bian, Z. Xu, J. Lu and Y. Y. Li, *ACS Appl. Energy Mater.*, 2020, **3**, 6087–6092.
48 D. Yu, Y. Zhang, F. Wang and J. Dai, *RSC Adv.*, 2021, **11**, 2307–2314.
49 L. Andronic and A. Enesca, *Front. Chem.*, 2020, **8**, 565489.
50 T. Wu, G. Sun, W. Lu, L. Zhao, A. Mauger, C. M. Julien, L. Sun, H. Xie and J. Liu, *Electrochim. Acta*, 2020, **353**, 136529.
51 L. F. Plaça, P.-L. S. Vital, L. E. Gomes, A. C. Roveda Jr, D. R. Cardoso, C. A. Martins and H. Wender, *ACS Appl. Mater. Interfaces*, 2022, **15**, 43259–43271.
52 F. Li, S. Wang, H. Yin, Y. Chen, Y. Zhou, J. Huang and S. Ai, *ACS Sens.*, 2020, **5**, 1092–1101.
53 N. Rahman, M. Nasir, A. A. Alothman, A. M. Al-Enizi, M. Ubaidullah and S. F. Shaikh, *J. King Saud Univ., Sci.*, 2021, **33**, 101280.
54 X. Chen, L. Liu, P. Y. Yu and S. S. Mao, *Science*, 2011, **331**, 746–750.
55 X. Liu, P. Carvalho, M. N. Getz, T. Norby and A. Chatzitakis, *J. Phys. Chem. C*, 2019, **123**, 21931–21940.
56 X. Lu, G. Wang, T. Zhai, M. Yu, J. Gan, Y. Tong and Y. Li, *Nano Lett.*, 2012, **12**, 1690–1696.
57 M. Plodinec, I. Grčić, M. G. Willinger, A. Hammud, X. Huang, I. Panžić and A. Gajović, *J. Alloys Compd.*, 2019, **776**, 883–896.
58 H. Zhou and Y. Zhang, *J. Phys. Chem. C*, 2014, **118**, 5626–5636.
59 I. Heng, C. W. Lai, J. C. Juan, A. Numan, J. Iqbal and E. Y. L. Teo, *Ceram. Int.*, 2019, **45**, 4990–5000.
60 Q. Wang, M. Li and Z. Wang, *RSC Adv.*, 2019, **9**, 7811–7817.
61 L. Fornasini, S. Scaravonati, G. Magnani, A. Morenghi, M. Sidoli, D. Bersani, G. Bertoni, L. Aversa, R. Verucchi and M. Riccò, *Carbon*, 2021, **176**, 296–306.
62 C. C. Raj, V. Srimurugan, R. Sundheep and N. Lakshman, *Inorg. Chem. Commun.*, 2023, **148**, 110286.
63 A. H. Anwer, F. Abdulaziz, S. Latif, A. Alanazi, S. Sultana and M. Z. Khan, *Mater. Sci. Eng., B*, 2023, **291**, 116367.
64 R. Liu, W. Guo, B. Sun, J. Pang, M. Pei and G. Zhou, *Electrochim. Acta*, 2015, **156**, 274–282.
65 A. Ramadoss and S. J. Kim, *Carbon*, 2013, **63**, 434–445.
66 Y. Qiao, J. He, Y. Zhou, S. Wu, X. Li, G. Jiang, G. Jiang, M. Demir and P. Ma, *ACS Appl. Mater. Interfaces*, 2023, **15**, 52381–52391.
67 L. Liu, G. Liu, S. Wu, J. He, Y. Zhou, M. Demir, R. Huang, Z. Ruan, G. Jiang and P. Ma, *Ceram. Int.*, 2024, **50**, 1970–1980.
68 R. Y. Hu, L. Y. Liu, J. H. He, Y. Zhou, S. B. Wu, M. X. Zheng, M. Demir and P. P. Ma, *J. Energy Storage*, 2023, **72**, 108656.
69 Z. Jiao, Y. Chen, M. Du, M. Demir, F. Yan, Y. Zhang, C. Wang, M. Gu, X. Zhang and J. Zou, *J. Alloys Compd.*, 2023, **958**, 170489.
70 R. H. Xu, P. P. Ma, G. F. Liu, Y. Qiao, R. Y. Hu, L. Y. Liu, M. Demir and G. H. Jiang, *Energy Fuels*, 2023, **37**, 6158–6167.
71 C. Xiang, M. Li, M. Zhi, A. Manivannan and N. Wu, *J. Mater. Chem.*, 2012, **22**, 19161–19167.
72 X. Sun, M. Xie, G. Wang, H. Sun, A. S. Cavanagh, J. J. Travis, S. M. George and J. Lian, *J. Electrochem. Soc.*, 2012, **159**, A364.
73 D. Yangbin, B. Wei, S. Jinhua, W. Yu, W. Chao, L. Chengbin, H. Yong and G. Jianxin, *ACS Appl. Mater. Interfaces*, 2016, **8**, 12165–12175.
74 H. Yin, S. Zhao, J. Wan, H. Tang, L. Chang, L. He, H. Zhao, Y. Gao and Z. Tang, *Adv. Mater.*, 2013, **25**, 6270–6276.
75 H. Kim, M. Y. Cho, M. H. Kim, K. Y. Park, H. Gwon, Y. Lee, K. C. Roh and K. Kang, *Adv. Energy Mater.*, 2013, **3**, 1500–1506.
76 Z. Zhang, F. Xiao, Y. Guo, S. Wang and Y. Liu, *ACS Appl. Mater. Interfaces*, 2013, **5**, 2227–2233.
77 S. Yang, Y. Lin, X. Song, P. Zhang and L. Gao, *ACS Appl. Mater. Interfaces*, 2015, **7**, 17884–17892.
78 V. H. Pham, T.-D. Nguyen-Phan, X. Tong, B. Rajagopalan, J. S. Chung and J. H. Dickerson, *Carbon*, 2018, **126**, 135–144.
79 J. M. Macak, B. G. Gong, M. Hueppe and P. Schmuki, *Adv. Mater.*, 2007, **19**, 3027–3031.
80 L. A. Lyon and J. T. Hupp, *J. Phys. Chem. B*, 1999, **103**, 4623–4628.
81 J. Gao, J. Xue, S. Jia, Q. Shen, X. Zhang, H. Jia, X. Liu, Q. Li and Y. Wu, *ACS Appl. Mater. Interfaces*, 2021, **13**, 18758–18771.
82 T. S. Rajaraman, S. P. Parikh and V. G. Gandhi, *Chem. Eng. J.*, 2020, **389**, 123918.
83 S. Kalathil, M. M. Khan, S. A. Ansari, J. Lee and M. H. Cho, *Nanoscale*, 2013, **5**, 6323–6326.
84 S. Sharma and P. Chand, *Results Chem.*, 2023, **5**, 100885.
85 H. Zhang, L. Lin, B. Wu and N. Hu, *J. Power Sources*, 2020, **476**, 228527.
86 K. G. Gallagher, S. E. Trask, C. Bauer, T. Woehrle, S. F. Lux, M. Tschech, P. Lamp, B. J. Polzin, S. Ha and B. Long, *J. Electrochem. Soc.*, 2015, **163**, A138.
87 L. M. Peter, *Electrochemical Impedance Spectroscopy and Related Techniques*, 2023.
88 Z. Zhang, Y. Yuan, L. Liang, Y. Cheng, H. Xu, G. Shi and L. Jin, *Thin Solid Films*, 2008, **516**, 8663–8667.
89 J. A. Castro, R. Quintero-Torres, N. R. de Tacconi, K. Rajeshwar and W. Chanmanee, *J. Electrochem. Soc.*, 2010, **158**, D84.
90 T. Hecht, H. Winter, A. Borisov, J. Gauyacq and A. Kazansky, *Phys. Rev. Lett.*, 2000, **84**, 2517.
91 Q. Wang, X. Zong, L. Tian, Y. Han, Y. Ding, C. Xu, R. Tao and X. Fan, *ChemSusChem*, 2022, **15**, e202102377.
92 S. Yang, Y. Li, J. Sun and B. Cao, *J. Power Sources*, 2019, **431**, 220–225.
93 M. Machreki, T. Chouki, G. Tyuliev, D. A. Žigon, B. Ohtani, A. Loukanov, P. Stefanov and S. Emin, *ACS Omega*, 2023, **8**, 21605–21617.